Clim Dyn (2017) 48:1089–1108
DOI 10.1007/s00382-016-3129-0

A multi-model ensemble view of winter heat flux dynamics and the dipole mode in the Mediterranean Sea

Giovanni Liguori[1,2] · Emanuele Di Lorenzo[1] · William Cabos[2]

Received: 13 September 2014 / Accepted: 13 April 2016 / Published online: 25 April 2016
© Springer-Verlag Berlin Heidelberg 2016

Abstract Changes in surface heat fluxes affect several climate processes controlling the Mediterranean climate. These include the winter formation of deep waters, which is the primary driver of the Mediterranean Sea overturning circulation. Previous studies that characterize the spatial and temporal variability of surface heat flux anomalies over the basin reveal the existence of two statistically dominant patterns of variability: a monopole of uniform sign and an east–west dipole of opposite signs. In this work, we use the 12 regional climate model ensemble from the EU-FP6 ENSEMBLES project to diagnose the large-scale atmospheric processes that control the variability of heat fluxes over the Mediterranean Sea from interannual to decadal timescales (here defined as timescales > 6 year). Our findings suggest that while the monopole structure captures variability in the winter-to-winter domain-average net heat flux, the dipole pattern tracks changes in the Mediterranean climate that are connected to the East Atlantic/Western Russia (EA/WR) atmospheric teleconnection pattern. Furthermore, while the monopole exhibits significant differences in the spatial structure across the multi-model ensemble, the dipole pattern is very robust and more clearly identifiable in the anomaly maps of individual years. A heat budget analysis of the dipole pattern reveals that changes in winds associated with the EA/WR pattern exert dominant control through both a direct effect on the latent heat flux (i.e., wind speed) and an indirect effect through specific humidity (e.g., wind advection). A simple reconstruction of the heat flux variability over the deep-water formation regions of the Gulf of Lion and the Aegean Sea reveals that the combination of the monopole and dipole time series explains over 90 % of the heat flux variance in these regions. Given the important role that surface heat flux anomalies play in deep-water formation and the regional climate, improving our knowledge on the dynamics controlling the leading modes of heat flux variability may enhance our predictability of the climate of the Mediterranean area.

Keywords Air-sea heat fluxes · Winter climate variability · Modes of climate variability · Mediterranean Sea climate · ENSEMBLES project

1 Introduction

The Mediterranean Sea is a morphologically complex basin where intense local air-sea interactions together with the inflow of Atlantic water drive Mediterranean overturning circulation. Among the air-sea interactions, anomalies in the surface net heat flux (NHF) play a crucial role in the climate of the region (Haines and Wu 1995; Madec et al. 1991; Roether et al. 1996; Theocharis et al. 1999), particularly in the formation of intermediate and deep-water masses, a process of fundamental importance for regional- and global-scale meridional overturning circulation (Artale et al. 2006; Calmanti et al. 2006; Josey 2003; Rahmstorf 1996, 1998). Therefore, to enhance our understanding of climate in this area, we must also improve our understanding of the air-sea exchange variability of NHF.

The influence of large-scale atmospheric circulation on the air-sea NHF variability over the Mediterranean region

✉ Giovanni Liguori
giovanni.liguori@gatech.edu

1 School of Earth and Atmospherics Sciences, Georgia Institute of Technology, Atlanta, GA 30332, USA

2 Departamento de Física, Universidad de Alcalá, 28801 Alcalá de Henares, Madrid, Spain

is well represented by several relevant teleconnection patterns in this region (Josey et al. 2011; OrtizBevia et al. 2012). The patterns with the greatest impact (see Fig. 3) are the North Atlantic Oscillation (NAO) (Hurrell 1995), the Eastern Atlantic (EA) pattern (Wallace and Gutzler 1981), the East Atlantic-Western Russia (EA/WR) pattern (Krichak et al. 2002), and the Scandinavian pattern (Bueh and Nakamura 2007). The NAO pattern is characterized by two opposite centers of action with anomalously high and low pressure over Azores and Iceland islands, respectively. This mode controls the strength and direction of westerly winds and storm tracks across the North Atlantic. The EA pattern is characterized by a broad low-pressure system centered to the west of the British Isles, which is approximately midway between the two centers of action of the NAO system. Negative phases of EA are associated with high pressure over the northern Atlantic and a relatively strong pressure gradient over the western Mediterranean. This pressure gradient produces a cold northerly airflow that enhances ocean heat loss over this region. The EA/WR pattern is characterized by three alternate-in-sign centers of action located in the northern Atlantic, central Europe, and western Russia. Positive values of EA/WR are associated with northerly/southerly winds in the eastern/western Mediterranean. Finally, the SCAN pattern presents, in its positive phase, a dipole structure with a low pressure over the Iberian Peninsula and a high pressure over northwestern Russia. In its positive phase, this mode promotes weak low pressure and southerlies over the entire Mediterranean Sea.

Josey et al. (2011) examined the impact of these modes on Mediterranean Sea surface heat flux during extreme seasons (i.e., summer and winter) and concluded that the NAO—the dominant mode of atmospheric variability in this region—has a minor impact on NHF variability compared to the EA and EA/WR patterns, which explain the largest fraction of NHF variability. Zveryaev and Hannachi (2011) found a direct link between the EA pattern and the leading mode of evaporation variability but no significant correlation with the EA/WR pattern. Papadopoulos et al. (2012b) identified two main responses of the NHF to the regional atmospheric teleconnection patterns: a uniform basin-wide response and an out-of-phase response in the western and eastern sub-basins, which we will refer to as the dipole pattern. While they found that the uniform response was attributed to the EA, the dipole pattern appeared to be a response to a combination of the first four modes of the Euro-Atlantic region (i.e., EA. EA/WR, NAO, and SCAN).

These previous analyses provide an understanding of the statistical and in some cases, mechanistic, relationships between NHF variability in the Mediterranean Basin and large-scale atmospheric modes. For instance, Josey et al. (2011) recognized that the EA mode has a coherent-basin-wide impact resulting from its associated northeasterly flow of cold dry air, which increases the air-sea humidity and temperature gradients and thus heat loss. The same work also connected the EA/WR mode with the heat flux anomalies of opposite signs in the eastern and western Mediterranean Basins. They hypothesized that this pattern occurs because the mode (EA/WR) drives a northerly flow of cold dry air over the eastern basin, enhancing heat loss, and a southerly flow of relatively warm moist air over the western basin, weakening heat loss. However, these studies focus on individual modeling or observational datasets to examine the spatial and temporal variability of surface heat fluxes. In this study, we use multiple observational datasets and 12 simulations of a multi-model ensemble to provide a more robust assessment of the statistical behavior of Mediterranean surface heat flux winter variability and to diagnose the mechanisms underlying links to the regional footprint of large-scale atmospheric teleconnection patterns. Moreover, this work is the first to assess the spatial and temporal variability of the Mediterranean air-sea heat fluxes in a multi-model ensemble of high-resolution regional climate models. Such model outputs, which are commonly used to investigate the climate over a specific region, may also be used as surface boundary conditions for hind-cast ocean simulations. In this regard, Herrmann and Somot (2008) have shown that a correct representation of air-sea heat fluxes is crucial to accurately modeling the key aspects of the Mediterranean Sea circulation such as the deep convection of the northwestern Mediterranean Sea.

Like many of the above-cited cited papers on the Mediterranean Sea heat flux variability, this paper focuses on the winter season. Studying the cold season has many advantages. For one, the formation of intermediate and deep water masses, which play a crucial role for the Mediterranean Sea circulation, is linked to air-sea heat flux exchanges occurring during the winter (Lascaratos et al. 1999). Additionally, winter anomalies dominate the annual mean heat budget (Josey et al. 2011), and extreme heat loss during this season has been linked to profound deep-water changes known as the Eastern Mediterranean Transient (Josey 2003). Furthermore, the influence of large-scale atmospheric modes on the Mediterranean climate is generally much stronger during the extreme seasons (i.e., winter and summer) than during the transition seasons (i.e., spring and fall). To examine the high- and low-frequency dynamics of heat flux variability in the Mediterranean Sea during the winter season, we combine two independent observational datasets with an ensemble of 12 high-resolution regional climate models. This work primarily focuses on the relationship between the two leading modes of winter NHF variability, which closely track the latent heat flux (LHF), and the climate of the Euro-Mediterranean region.

Section 2 presents the dataset and methodology for the computation of the leading modes of LHF variability and Sect. 3 a multi-model ensemble view of the spatial and temporal statistics of the modes. Section 4 analyzes the relationships between the modes and large-scale atmospheric forcing and Sect. 5 summarizes and discusses the results.

2 Dataset and methodology

2.1 The observational datasets

Before presenting the observational and modeling data used in this work, we would like to examine the relationship between NHF and LHF. NHF consists of a balance of four components of heat flux: LHF, sensible heat flux (SHF), longwave radiation (LWR), and shortwave radiation (SWR). The first two are turbulent while the last two are radiative. The estimation of these two kinds of heat fluxes involves measurements of different physical parameters, which are typically not available in observational datasets at the same spatial resolutions and temporal coverages. Table 1 shows the most commonly used observational datasets for both turbulent and radiative fluxes.

In this work, estimations of radiative fluxes come from a modified Mediterranean Sea version of the National Oceanography Centre 1.1 (NOC1.1—hereafter referred to as NOC) dataset (Josey et al. 1999). Estimations of turbulent fluxes come from two sources: the NOC dataset and the objectively analyzed air-sea fluxes (OAFlux). While the OAFlux dataset provides estimations for NHF, the NOC dataset does not, so we compute the NHF from its four heat-flux components. The NOC dataset is based on ship observations provided by the International Comprehensive Ocean–Atmosphere Data Set (ICOADS, Woodruff et al. 1998) and presented on a 1° × 1°. spatial grid for the period 1979 to 2004. The NOC dataset analyzed in our study is a modified version of the standard datasets computed using another formulation of the radiative flux components and analyzed by Josey et al. (2011). Specifically, the longwave flux is estimated by an improved formula calibrated with in situ measurements from the Mediterranean Sea (see Bignami et al. 1995). In addition, the shortwave flux has been corrected for aerosol loading following the method of Gilman and Garrett (1994). OAFlux is a 50-year global dataset on a 1° × 1° grid for the period 1958 to 2008. This product is a result of merging satellite observations with surface moorings, ship reports, and atmospheric model reanalysis data.

With the exception of the NOC dataset, which provides estimations at a 1° × 1° resolution and covers the same period for all four components of the surface heat flux, radiative fluxes are available for shorter periods and lower spatial resolution with respect to turbulent fluxes. For instance, the widely used International Satellite Cloud Climatology Project (ISCCP 2) dataset (Zhang et al. 2004) provides gridded estimations on a 2.5° × 2.5° horizontal resolution that cover the period 1984 to 2009. However, for the Mediterranean Sea, where important processes take place on a small scale, data with a spatial resolution of 2.5° × 2.5° are mainly useful for basin-integrated budget purposes (e.g., Sanchez-Gomez et al. 2011). Moreover, no estimations are available for radiative fluxes before 1980, and the longest period covered consists of 25 years (i.e., 1984–2009 for ISCCP 2), which limits possible inferences on low-frequency variability. Therefore, the ISCCP 2 dataset is not used in this study. In contrast, datasets of turbulent flux estimates often cover a longer period with a higher spatial resolution such as the 0.5° × 0.5° for the Hamburg ocean atmosphere parameters and fluxes from the satellite (HOAPS) dataset (Andersson et al. 2007) and 1° × 1° for the NOC and OAflux datasets. However, the HOAPS dataset has several limitations. In addition to its relatively short coverage, HOAPS does not cover the Adriatic Sea, the Aegean Sea, or some coastal regions. This lack of spatial coverage strongly affects our ability to study air-sea heat exchange, as explained in the introduction and further confirmed by the strong variance shown by the multi-model ensemble (see next section). For these reason, we select the NOC and OAflux for comparing the multi-model ensemble outputs to observational datasets.

Our analyses mainly focuses on air-sea heat fluxes; however, in Sect. 3, we also use sea-level pressure (SLP) from the ERA40 reanalysis (Uppala et al. 2005), and in Sect. 4.2, we also use 2 m air specific humidity and the SST from the OAflux database, and 10 m winds from the NCEP reanalysis (Kalnay et al. 1996). To examine the influence of large-scale atmospheric circulation on the variability of air-sea

Table 1 Observational datasets for the air-sea heat flux components

Variable	Dataset	Period	Resolution (°)
Radiative fluxes (SWR and LWR)	ISCCP2, **NOC**	1984–2008, **1980–2004**	2.5, **1**
Turbulent fluxes (SHF and LHF)	**OAFlux**, HOAPS, **NOC**	**1958–2008**, 1988–2005, **1980–2004**	**1**, 0.5, **1**
Net heat flux (NHF)	**OAFlux**, **NOC**	**1958–2008**, **1980–2004**	**1**, **1**

In bold, the datasets used in this work

heat fluxes over the Mediterranean region, we employ the NOAA Climate Prediction Centre (CPC) monthly mean values of the four prominent atmospheric modes of the Euro-Atlantic region (i.e., EA, EA/WR, NAO, and SCAN) for the period 1958 to 2010.

2.2 Regional climate model experiments

In addition to the above-presented observations, we use the multi-model dataset from the regional climate model experiments performed within the EU-FP6 ENSEMBLES project framework. In this work, we use 12 RCMs driven by the ERA40 reanalysis data and operating at a 25 km horizontal resolution. The models, which must cover a common minimum domain that includes the entire Mediterranean Sea, simulated the period 1961 to 2000. The RCMs differ for the model setup and the grid specifications such as the rotation grid, and the number of vertical levels. Table 2 lists more details about the experiments and the ENSEMBLES project website (http://ensemblesrt3.dmi.dk) provides more information regarding each model.

2.3 LHF as a proxy for NHF variability

In the open ocean, turbulent latent heat flux generally controls the variability of the NHF (Alexander et al. 2002). This finding also applies to the Mediterranean Sea (Garrett et al. 1993; Josey 2003; Josey et al. 2011; Papadopoulos et al. 2012a), especially during the boreal winter (December–January–February–March, hereafter DJFM) when the short-wave component becomes less important than it is during the summer (June–July–August–September, hereafter JJAS). Figure 1 shows maps of the winter mean and normalized standard deviation of NHF and LHF fields (A sign convention used is that fluxes out of the ocean are positive) for the multi-model ensemble and both observations, NOC and OAflux. These maps reveal different means but very similar normalized standard deviations in both observations and the multi-model ensemble mean (ENSm). We normalized the standard deviation by its maximum value in order to use the same color scale and highlight the strong similarity of the spatial structure of LHF and NHF variances.

Table 2 Summary of the main features of the RCM used in the EU-FP6 ENSEMBLES project

Institution	RCM	Vertical levels	References
CNRM	ALADIN	31	Radu et al. (2008)
C4I	RCA	31	Kjellström et al. (2005)
DMI	HIRHAM	31	Christensen et al. (1996)
ETHZ	CLM	21	Bhöm et al. (2006)
ICTP	RegCM	34	Giorgi and Mearns (1999)
KNMI	RACMO	40	Lenderink et al. (2003)
METNO	HIRHAM	31	Haugen and Haakensatd (2006)
METOHC	HadRM	19	Collins et al. (2006)
MPI	REMO	27	Jacob (2001)
SMHI	RCA	24	Kjellström et al. (2005)
UCLM	PROMES	28	Sanchez et al. (2004)
OURANOS	CRCM	28	Plummer et al. (2006)

Table adapted from Sanchez-Gomez et al. (2011)

Fig. 1 Spatial distribution of the temporal mean and normalized standard deviation of latent heat flux (LHF) and net heat flux (NHF) for the OAflux dataset, the NOC dataset, and the multi-model ensemble mean. The Period analyzed is 1961–2000 for RCM simulations and ENSm, 1980–2004 for NOC dataset, and 1958–2010 for OAflux dataset. A sign convention used is that fluxes into the ocean are positive. The Inter-model spread has been calculated as the standard deviation of the individual model climatological winter mean. Units are in [W/m^2] for the mean and the spread. The standard deviation has non-dimensional units as it has been normalized by its maximum value, which is indicated in each subfigure as "Max. σ"

This simple but fundamental analysis suggests that the winter NHF mean results from a combination of turbulent and radiative fluxes while its spatial variance, represented here by the standard deviation, is controlled by the LHF alone. Although both the mean and the standard deviation present significant differences, this result is valid for all of the analyzed datasets. ENSm and OAflux often present similar patterns while NOC shows somewhat different features. To identify regions with large inter-model uncertainties, we compute the spread among models as an inter-model standard deviation. This parameter, shown in Fig. 1, reveals a larger spread associated with the coastal region and the Aegean Sea for both NHF and LHF. This result was already noted by Sanchez-Gomez et al. (2011), which uses the same multi-model ensemble to analyze heat and fresh water budgets in the Mediterranean Sea. In this work, the authors suggested that the large spread in coastal regions and the land-enclosed basin (i.e., the Aegean Sea) are likely due to the difficulty in accurately representing processes related to the local wind fields, orography, and, in the case of the Aegean Sea, the locally increased internal variability of the RCMs.

Although Fig. 1a reveals that the spatial structures of winter LHF and NHF variances are similar, this does not assure similar variability of the two fields. However, a decomposition of the winter anomalies using empirical orthogonal functions (EOFs) and principal components (PCs) analysis reveals a close relationship between the spatial and temporal variability of NHF and LHF. The EOF/PC analysis decomposes the variance of the NHF and LHF into a dominant pattern of spatial variability (e.g., EOFs) and their associated temporal modulation (e.g., PCs). Figure 2a

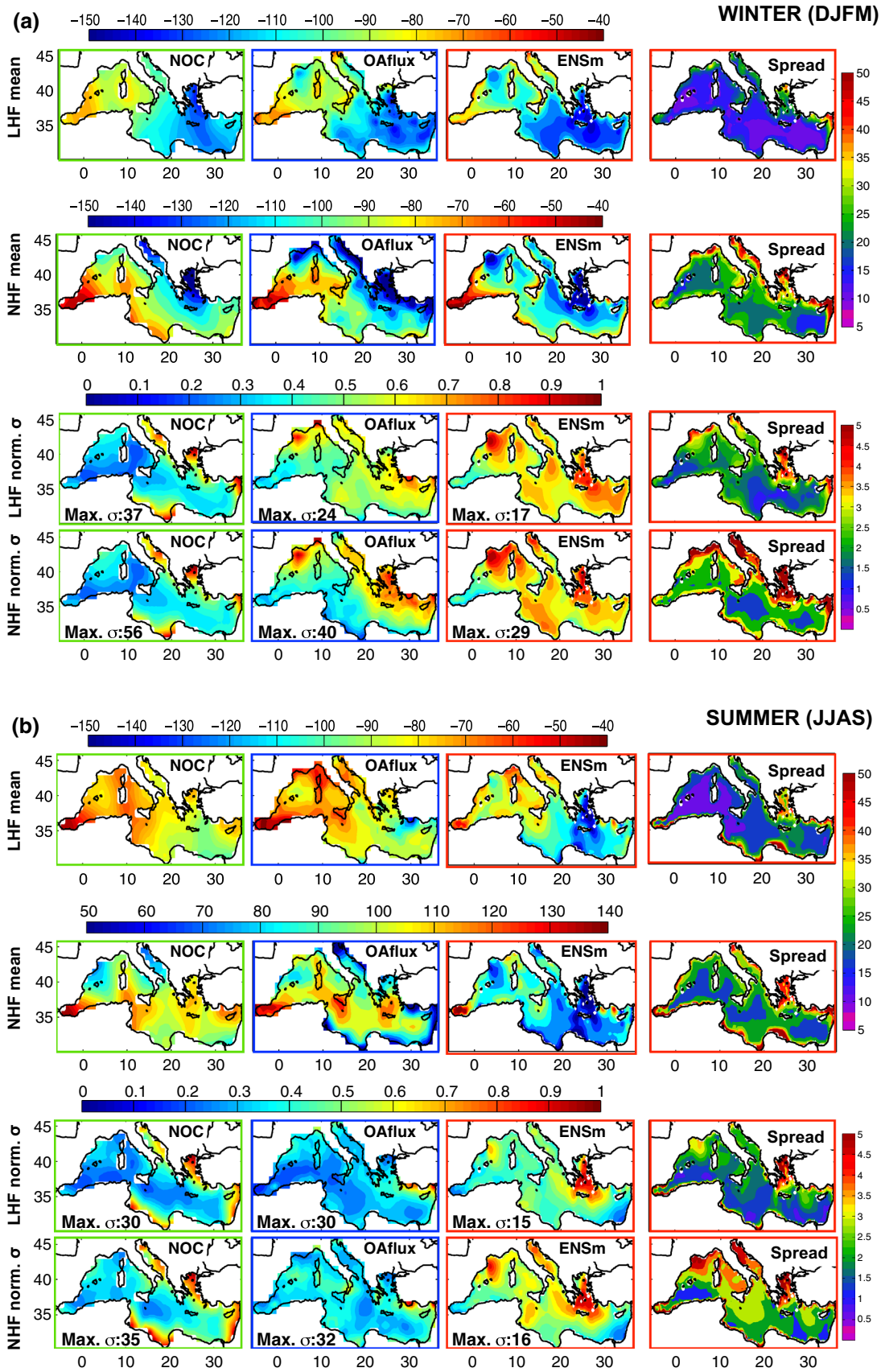
(a)
WINTER (DJFM)
LHF mean
NHF mean
LHF norm. σ
NHF norm. σ
NOC
OAflux
ENSm
Spread
Max. σ:37
Max. σ:24
Max. σ:17
Max. σ:56
Max. σ:40
Max. σ:29
(b)
SUMMER (JJAS)
Max. σ:30
Max. σ:30
Max. σ:15
Max. σ:35
Max. σ:32
Max. σ:16

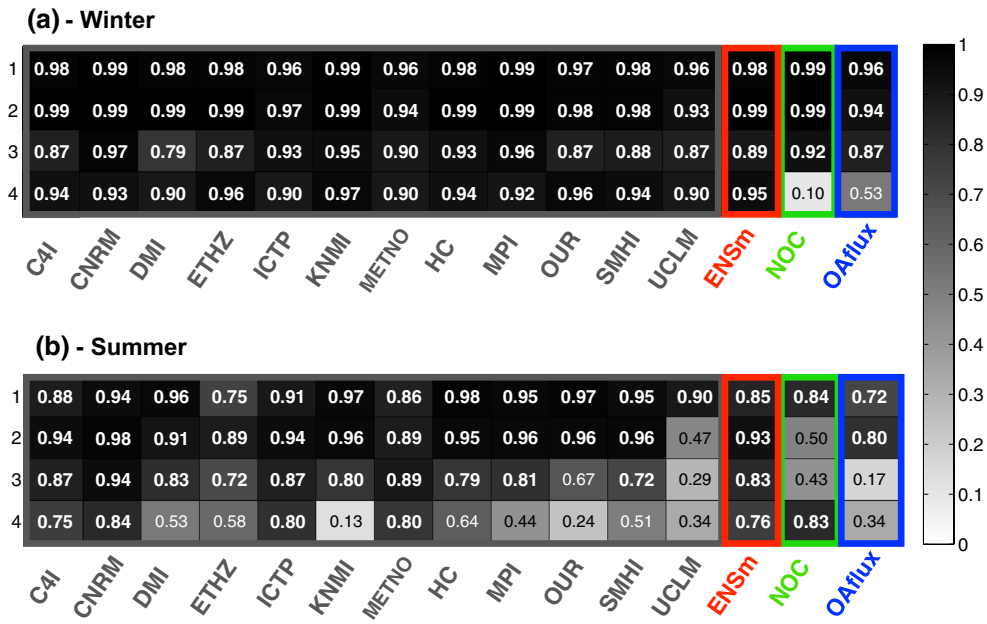

Fig. 2 *Panel* **a** shows the correlation coefficients for first 4 PCs between winter (DJFM) anomalies of NHF and LHF for the simulations, the multi-model ensemble mean (ENSm), the NOC and the OAflux datasets (*grey*, *red*, *green*, and *blue rectangles*, respectively). The *grey shading* indicates the absolute value of the correlation coefficient and *boldface* indicates a significant correlation at a 99 % level. The significance of the correlation coefficients throughout this paper are estimated by computing empirical probability distribution functions (EPDFs) for the correlation coefficient of two *red-noise* time series with the same lag-1 autoregression coefficients of those estimated in the original signals. The EPDF is used to assess significance levels of 95 and 99 %. In **b** the same analysis is performed using summer (JJAS) anomalies

shows the correlation coefficient (the methodology used to assess its statistical significance is explained in the caption of Fig. 2) between the first four PCs of NHF and LHF anomalies (i.e., NHFa and LHFa) during DJFM for the observational datasets, the simulations, and the ENSm (green, blue, and red rectangles, respectively). On average, the two leading modes explain about 77 % of the total variance. The correlations for the first two modes are generally very high and often close to one. For higher modes, the correlations slightly decrease, but they are considerably large even for the fourth mode. The uniquely low correlation value (i.e., PC4 of NOC) occurs when the order of the modes between LHF and NHF is inter-changed. In fact, when this occurs, the correlation is close to zero because of the orthogonality condition of the PCs. For instance, the correlation coefficient of LHF-PC4 and NHF-PC5 of NOC was about 0.90, confirming the expected change in the order of the PCs. The results shown in Fig. 2a demonstrate that at least during the winter and for the first few modes, LHF variability strongly captures variations in the NHF. As discussed in Sect. 2.1, LHF estimates cover longer periods with a higher spatial resolution with respect to NHF estimates. Therefore, for the remainder of the analyses, we focus on winter LHF to diagnose the dynamics controlling the variability of the winter NHF. Last, we would like to conclude this section by pointing out that at least for the first two modes and especially for the RCMs, this close relationship between the LHF and NHF also holds, to some extent, during the summer season (Fig. 2b).

3 Statistical analysis of the leading modes of LHF

To investigate the spatial and temporal structure of the interannual variability of Mediterranean LHFa during the boreal winter (DJFM), we perform an EOF analysis of the winter mean latent heat flux for both models and observations. In this paper before analyzing any dataset, we remove a linear trend for each grid point and for each time series (i.e., CPC indices). We restrict our statistical analysis to the first two leading modes, as they explain most of the observed variability (in average 77 % of the total variance). The steps of the analysis include (a) a description of the EOF structures, (b) a comparison between the models and observations, and (c) a correlation analysis of the PC1 and PC2 with known large-scale atmospheric teleconnection patterns (i.e., NAO, EA, EA/WR, and SCAN).

To characterize the temporal scales at which these teleconnections are more active, we also analyze the correlations for the low- and high-pass filtered PCs (below and above a period of 6 years). Finally, by comparing the results of the models and observations, we assess the capability of

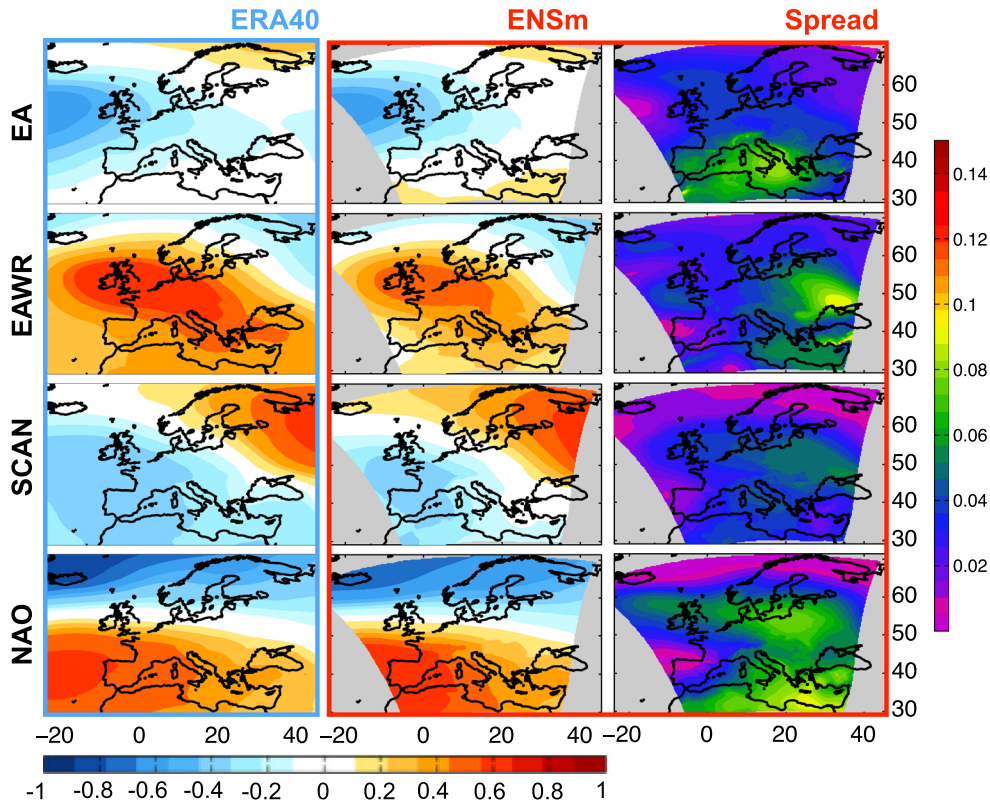

Fig. 3 Correlation maps between indices of atmospheric variability and SLP during winter season (DJFM) for ERA40 (*left column*) and multi-model ensemble mean (ENSm; *middle column*). The figure shows also the inter-model spread (*right column*) calculated as in Fig. 1

RCMs to represent the atmospheric teleconnections dynamics that affect LHF variability. To present the employed climatic indices and their relationship with the atmospheric circulation, we compute the correlation maps (Fig. 3) between the indices and the SLP of the multi-model ensemble mean and the ERA40 reanalysis. We choose the ERA40 observational dataset since it has been used to drive the multi-model ensemble simulations, and thus it is important that the consistency between the large-scale features of the dynamical downscaling and of the forcing fields be checked. In addition to the correlation maps, we compute the inter-model spread to identify regions with large uncertainties among the models. Figure 3 shows the correlation maps between the indices and the SLP of the ERA40 reanalysis and of the multi-model ensemble mean along with the spread, as defined in Fig. 1.

Figure 3 reveals strong consistency between the multi-model ensemble mean and the ERA40 reanalysis. For all the analyzed climatic indices, the correlation map for ENSm is similar to that obtained for ERA40. One minor but noteworthy difference is the slightly smaller correlation for the center of action of the EA/WR mode in the multi-model ensemble mean. As the center of action of this mode is located far from the prescribed lateral boundary conditions, it is weakly influenced by the driving field and therefore more prone to revealing differences in the model dynamics. The inter-model spread (last column) shows generally low values over the centers of action, again confirming that most of the models closely represent these atmospheric modes. Regions of high inter-model spread are mostly located in the eastern part of the domain since the prevalent westerly flow, which characterizes the circulation of the region, exerts control from the western lateral boundary that decreases as it moves eastward. Moreover, except for NAO, which also shows a high spread over the northern Africa and eastern Mediterranean regions, high-spread areas are mostly over regions of low correlation, which can be partially explained by the weak atmospheric mode in regions where the internal variability of the models dominates the signal.

3.1 First mode

Figure 4 shows the first mode of the LHFa for both models and observations. The first four rows show the RCM fields while the fifth row presents the two independent observational datasets, NOC and OAflux, and the multi-model ensemble mean (ENSm). In addition to the spatial pattern, each subfigure also shows the amount of explained variance and the temporal/spatial correlation between the associated PC1/EOF1 and OAflux PC1/EOF1. Before examining the spatial structure of the patterns, we report the explained variance for both models and observations. For RCMs, the explained variance associated with the first

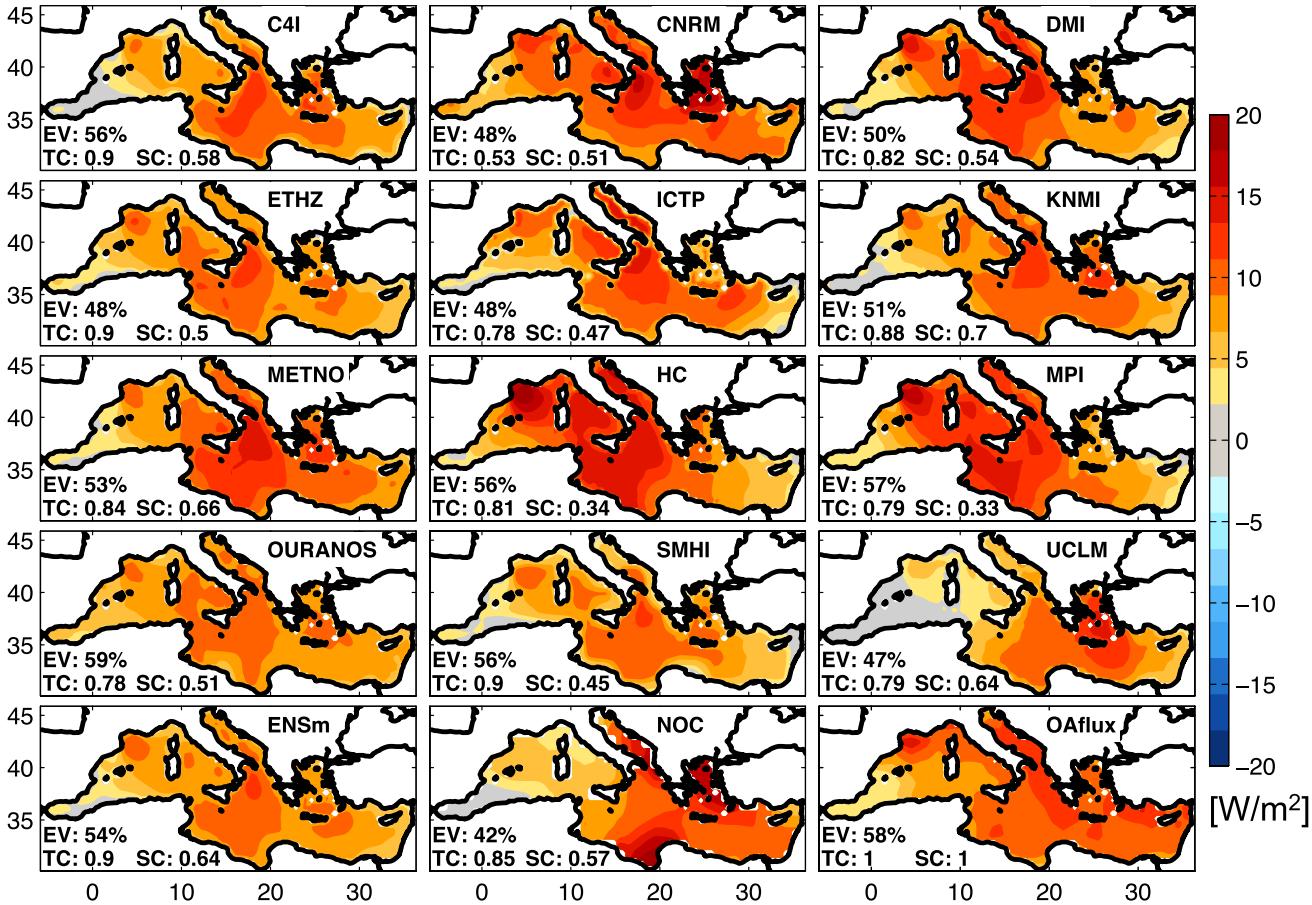

Fig. 4 Spatial patterns of the first mode (EOF1) of the winter mean LHFa for the observational datasets, the simulations, and the multi-model ensemble. Each *subfigure* also indicates the amount of explained variance (EV), and the values of the spatial and temporal correlation (SC and TC, respectively) between the simulated mode and the OAflux mode. The SC (TC) is obtained computing the spatial (temporal) correlation between the simulated and observed EOF1 (PC1). Units are [W/m^2]

mode ranges from a minimum of 47 % for UCLM to a maximum of 59 % for OURANOS. The average value is 52 %, and the associated standard deviation is 6 %. For the observations, the explained variance is 42 % for the NOC and 58 % for the OAflux, which reveals a range similar to the one find in the models even though we analyzed only two datasets. Thus, the amount of explained variance for each RCM is consistent with the uncertainty of the observations.

The spatial pattern of EOF1 for both models and observations (Fig. 4) reflects coherent same-sign variations of LHF over the entire Mediterranean Basin. Despite some differences in the spatial representation of the EOF 1 that are also evident in the two observational datasets, the models and observations share important features such as large values of the loadings in the Gulf of Lion and the Ionian Sea and small loading values in the western-most region of the basin in the Alboran Sea. Both the Gulf of Lion and the Ionian Sea are locations of deep-water formation (Roether et al. 2007; Schroeder et al. 2008), and their appearance in the first mode is not surprising because they are characterized by intense LHF variations at inter-seasonal and annual timescales.

To evaluate the multi-model ensemble skills in reproducing the observed variability associated with the first mode, we have computed the correlations between PC1 of each RCM and OAflux. These correlations (Fig. 4) are generally very high with a mean value of 0.81 and a maximum of 0.90 for the ENSm. Physically, the PC1 time series represents the variability of the basin-averaged winter LHFa. For both observations and simulations, represented here by the multi-model ensemble mean along with the inter-model spread, Fig. 5 shows the PC1 time series against the basin-averaged winter LHFa time series. This figure reveals how PC1 nearly parallels the basin-averaged mean value with correlation coefficients as high as 0.99 for both observations and simulations. Therefore, we conclude that the multi-model ensemble is able to capture the temporal

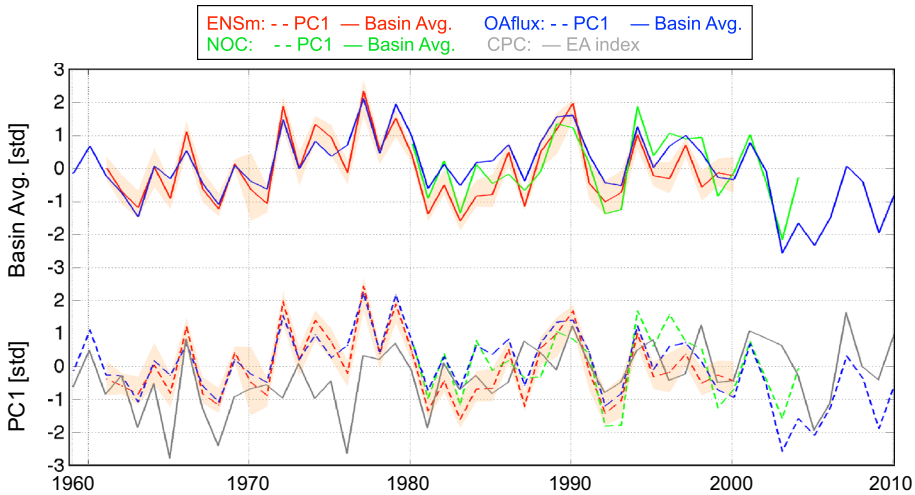

Fig. 5 Time series of normalized PC1 (*Solid line*) and normalized basin-averaged winter LHF anomalies (*Dashed line*) for ENSm (in *red*), NOC, (in *green*), and OAflux (in *blue*). In the lower part the PC1 s are compared with the EA index (*grey line*). The *red shading*, representing the inter-model spread, has been calculated as the standard deviation of the individual model value of the PC1 and of the basin-averaged winter LHF anomaly. All time series are normalized by their standard deviations therefore units are in standard deviations (SD)

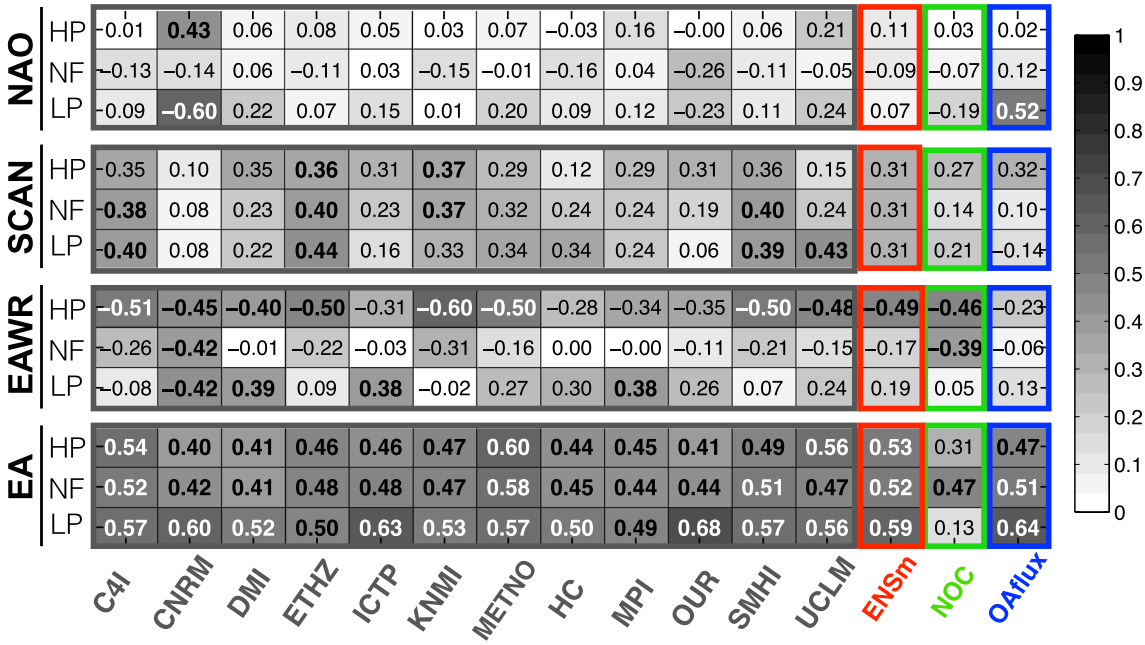

Fig. 6 Values of the correlation coefficient between the winter (DJFM) LHFa-PC1 time series and the corresponding winter indices of the four main atmospheric modes. The Period analyzed is 1961–2000 for RCM simulations and ENSm (respectively *grey* and *red rectangles*), 1980–2004 for NOC dataset (*green rectangle*), and 1958–2010 for OAflux dataset (*blue rectangle*). The *grey shading* indicates the absolute value of the correlation coefficient and *boldface* indicates a significant correlation at a 99 % level. In addition to the non-filtered (NF) time series we also analyzed high-pass (HP) and low-pass (LP) filtered time series. For the high- and low-frequency analysis, we retained Fourier components shorter and longer than a 6-year period, respectively

variability of the first mode despite some differences in the spatial patterns of the individual models that likely reflect uncertainty associated with regional expressions of the large-scale dynamics of basin-wide warming and cooling.

3.1.1 Interannual to decadal links to the regional climate

The EOF analyses of spatial modes (Fig. 4) show relatively inconsistent patterns among the models, which are able to

track a high correlation with observations in time. Now, we examine the links between the leading mode of variability of the Mediterranean latent heat flux and the patterns of regional atmospheric circulation. We compute the correlations between the leading PCs and the four climate indices (i.e., NAO, EA, EA/WR and the SCAN) with larger impact on the Mediterranean region. Moreover, to characterize the temporal scales at which these teleconnections are active, we analyze high- and low-pass filtered time series. The filtering method that we use is a simple Fourier filter. After performing an FFT analysis, we reconstruct the time series using only selected Fourier components. In particular, for the high- and low-frequency analyses, we retain Fourier components that are shorter and longer than a 6-year period, respectively. With the aim of separate interannual (1–6 year) and decadal (8–12 year) timescales, we decided, after performing some sensitivity tests, to choose 6 years as the threshold at which we separate these scales. Figure 6 shows the correlations for the non-filtered (NF) time series as well as for the high-passed (HP) and low-passed (LP) time series. The boldfaced numbers in Fig. 6 indicate a significant correlation at a 99 % level.

In agreement with previous studies of Josey et al. (2011), Zveryaev, and Hannachi (2011), the first mode is highly correlated with the EA mode (see also Fig. 5, bottom time series). The NF correlations reveal that, except for two RCMs (i.e., CNRS and DMI), all models show noteworthy correlations above 0.44 with a value of 0.52 for the ENSm, which is very close to the correlation found for the OAflux dataset. The connection between the EA mode and the heat fluxes over the Mediterranean Sea can be summarized as follows: the negative phases of EA are associated with anticyclonic circulation centered over the northern Atlantic and a relatively strong pressure gradient over the western Mediterranean that produces a cold northerly airflow, which, in turn, enhances ocean heat loss over this region. However, the correlation maps in Papadopoulos et al. (2012a, b) show that the LHFa in the westernmost part of the basin is mostly independent from the EA mode, which is consistent with the low value of the first mode loading over this region. Although we remove a linear trend for each grid point from the dataset before performing the EOF analysis, the PC1 shows strong multi-decadal variability that result in a negative trend after 1990, which is not present in the EA time series (Fig. 5). Previous studies have already reported such a trend in the Mediterranean Sea LHF, which has been attributed to SST-driven changes in the surface humidity gradient linked to global warming (Mariotti 2010; Skliris et al. 2011). The EA represents a large-scale atmospheric mode of variability, but it does not capture these basin-scale signals (e.g., the LHF trend).

An examination of filtered time series correlations reveals a noteworthy feature of the PC1-EA relationship: except for NOC, the correlation is slightly enhanced by the low-pass filter. Although not present in the OAflux dataset, Fig. 6 reveals an interesting high-frequency correlation between the PC1 and the EA/WR mode in most of the models, the ENSm, and the NOC dataset. Regarding the other regional climate indices, that is, the NAO and SCAN indices, Fig. 6 reveals low correlations, mostly below the significance level. While the NAO index presents a significant correlation only for the LP time series of OAflux and CNRM, the SCAN presents significant correlation only for few RCMs. These analyses confirmed the PC1-EA relationship and revealed a slight increase in this teleconnection at periods >6 years. Although rather speculative, these analyses also suggest a high frequency (i.e., periods <6 years) relationship between the PC1 and the EA/WR mode.

3.2 Second mode

Unlike the first mode, the spatial pattern of the second mode shows strong consistency among the models and the observations (Fig. 7). For instance, the spatial correlation between the RCMs and the OAflux is generally strong, ranging from a minimum of 0.92 for ICTP to a maximum of 0.97 for MPI. This mode is characterized by a well-defined dipole structure that represents opposite variations of LHF in the eastern and western parts of the Mediterranean Sea. While the positive pole of the dipole structure is almost always located in the GOL region, the negative pole is not always located in the same region. The negative pole is often located in the Aegean Sea, but in many cases, it appears to be spread between two locations, the Aegean Sea and the area south of Cyprus (Fig. 7). Moreover, the slightly diverse character of NOC, which does not show any clear pole in the Eastern basin, is worth mentioning. Compared to the first mode, the explained variance of the second mode shows a remarkable difference between RCMs and observations. While the explained variance for the RCMs is always above 24 %, with most of the models around 26 %, the explained variance for the observations is smaller, 20 % for OAflux and only 16 % for NOC. The PC2 time series for the observational datasets are always significantly correlated with those of the models (Fig. 8). Excluding CNRS, the correlation is always above 0.63 with an average value of 0.75 and a maximum value of 0.83 (C4I).

3.2.1 Interannual to decadal links to the regional climate

We examine the links between PC2 and the four atmospheric climate modes, shown in Fig. 9. Except for several RCMs and the NOC dataset, the NF time series reveal significant correlations between the PC2 and the EA/WR index, ranging from 0.38 to 0.53 (the time series of the PC2 and the EA/WR index are shown in Fig. 8). Moreover,

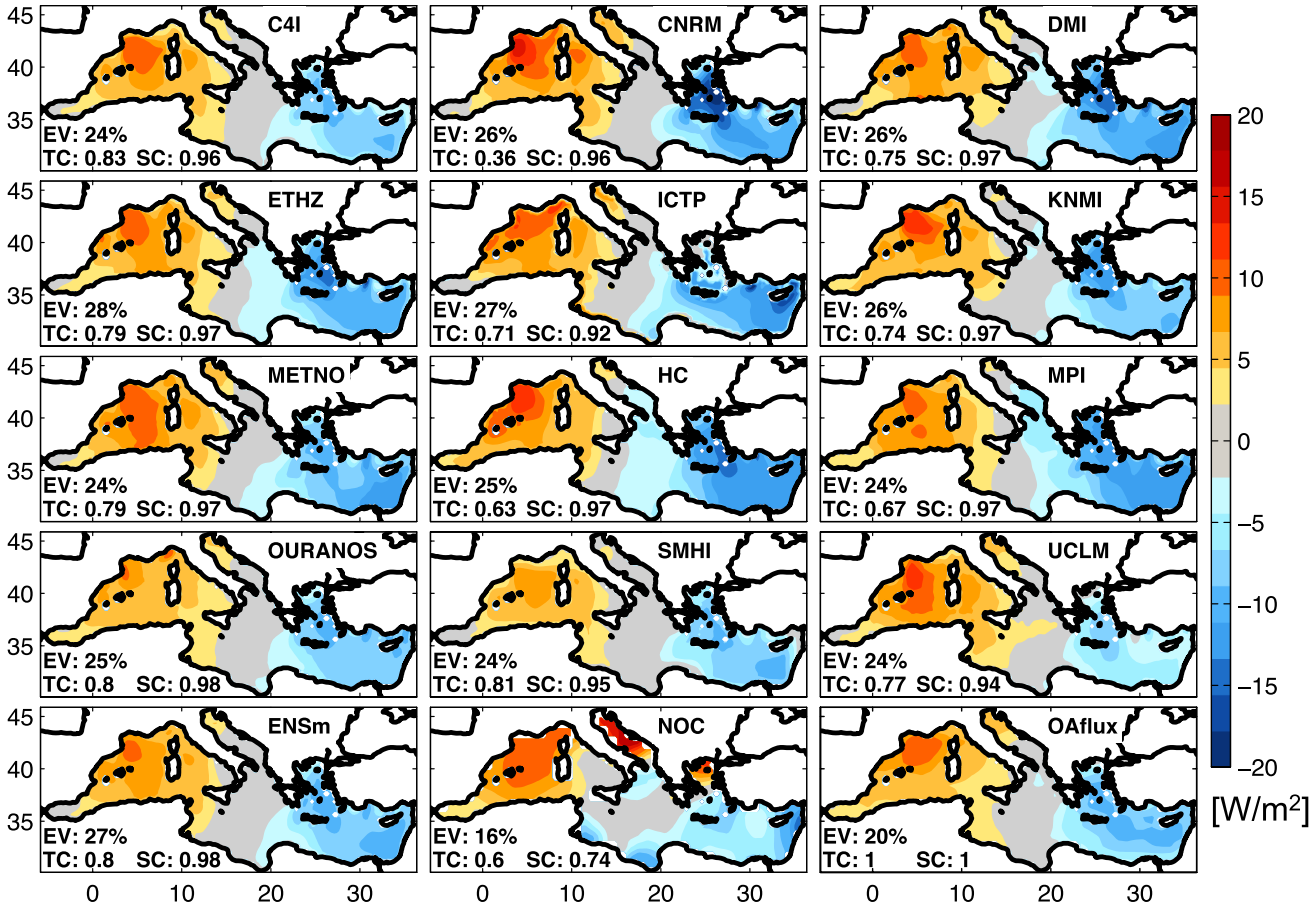

Fig. 7 The same as Fig. 4, but for the second mode

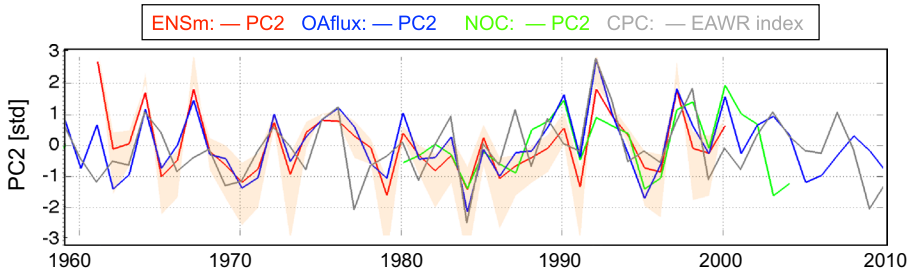

Fig. 8 Time series of normalized PC2 for ENSm (in *red*), NOC, (in *green*), and OAflux (in *blue*). The *grey line* is the EA/WR index. The *red shading*, representing the inter-model spread, has been calculated as the standard deviation of the individual model value of the PC1 and of the basin-averaged winter LHF anomaly. All time series are normalized by their standard deviations therefore units are in standard deviations (SD)

the analyses of the low- and high- frequency-filtered time series (Fig. 9) reveal that this correlation is significantly enhanced by the low-pass filter with average correlation coefficients of about 0.68. Josey et al. (2011) were the first to recognize the influence of the EA/WR in the analysis of a NCEP/NCAR and ARPERA datasets. They showed that the EA/WR mode is associated with an east–west dipole structure in the heat exchange, which is characterized by an approximately equal opposite signal of about 15 Wm^{-2}. However, as noted by others (Papadopoulos et al. 2012b), the time series of the PC2 is also connected to other teleconnection patterns in this region. To better understand the large-scale dynamics underlying the expression of this dipole mode (DM), we conduct a diagnostic and budget analysis of the LHF dipole during the period when this mode is most active.

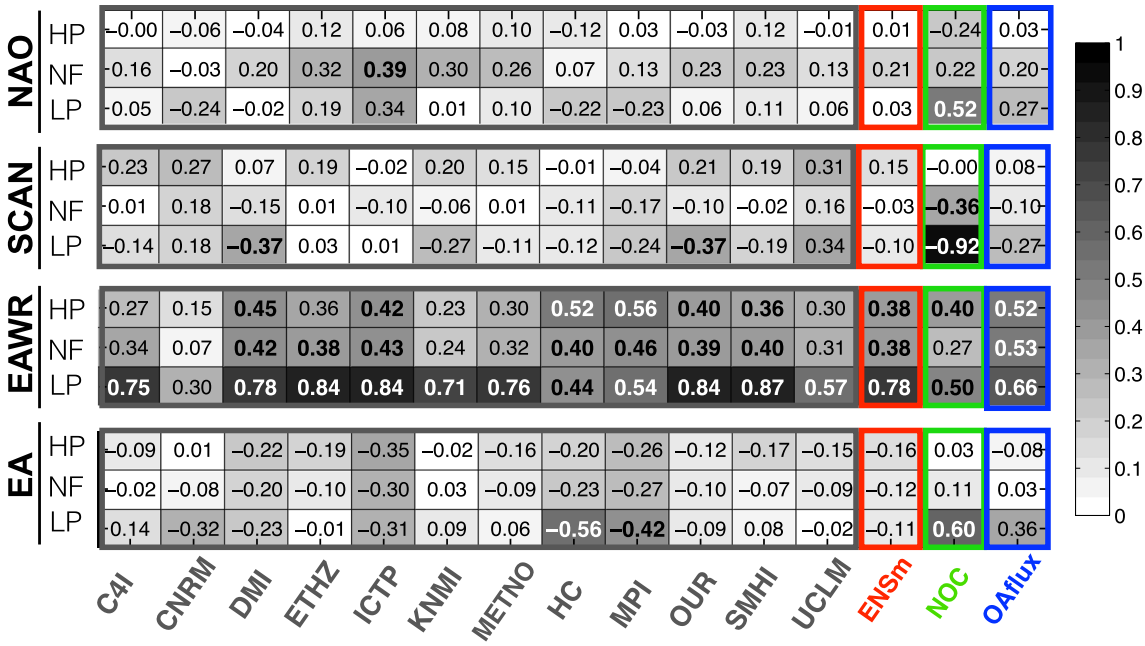

Fig. 9 The same as Fig. 6, but for PC2

4 Decomposing the temporal and spatial dynamics of the dipole mode

As statistically derived modes are constrained to be orthogonal while physical modes may show some interdependence, they do not always reflect real physical modes (Simmons et al. 1983). Thus, the physical interpretation of the statistically derived modes (e.g., DM) can be controversial (Dommenget and Latif 2003). Furthermore, a close explained variance of higher order EOFs might indicate that two or more EOFs capture oscillations or propagation dynamics in the physical field. To determine if the variance associated with the DM (EOF2) is statistically distinct from the variance associated with higher modes, we compute the uncertainties of each eigenvalue using North's rule (North et al. 1982). This analysis reveals that PC1 and PC2 (i.e., DM) have well-separated eigenvalues at the 95 % significance level in OAflux and ENSm, but not in NOC, which has overlapping second and third eigenvalues. This last result may partially explain why the EOF2 of NOC shows a relatively distinct pattern among all of the analyzed datasets (see Fig. 7). The statistical significance of the DM (EOF2) does not guarantee the existence of a real physical mode. Moreover, the explained variance of the DM is about one-third of the variance explained by the first mode, and therefore, even if it is a real structure, the dipole may not be physically relevant. Therefore, we dedicate this section to assess the relevance, the physical meaning, and the dynamics of the DM.

4.1 Is the dipole structure a relevant feature in the Mediterranean?

The first issue we wish to address is whether the DM represents a real feature of the Mediterranean climate. To answer this question, we examine how often the first and second mode (i.e., the monopole and the dipole) structures occur in the winter anomalies of the raw data. To this end, we compute the spatial correlation between each mode and the winter anomalies of LHF for both models and observations (Fig. 10). We find that while EOF1 explains most of the variance in the LHF, it is EOF2 (the DM) that occurs more frequently in the anomaly structure in both observations and models (e.g., the ENSm). While EOF1 captures strong interannual events and tracks the large-scale mean, EOF2 captures the recurring spatial pattern, which often emerges as a dipole structure. Although this spatially predominant role of the DM occurs in all the analyzed datasets, we should note several important differences. First, OAflux and ENSm show similar correlations, which is consistent with the strong correlations between their first two modes (see Sect. 3). In contrast, NOC shows no clear dominance of EOF2 in the spatial structure and misses the peaks of correlations above 0.80, which characterizes the EOF2 of OAFlux and ENSm.

Another feature in Fig. 10 worth noting is related to the OAflux correlations series in the period 2000 to 2010. Starting from the year 1998, the first mode becomes dominant, and the dipole correlation does not exceed 0.55. This

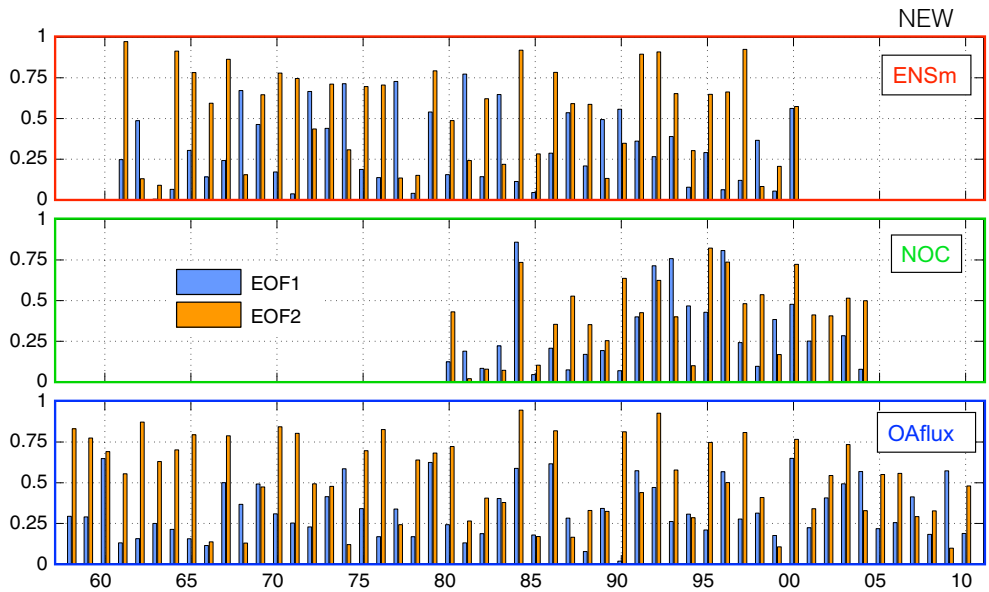

Fig. 10 Values of the spatial correlation coefficient between the winter mean LHFa pattern and the corresponding two leading EOFs for ENSm (1961–2000), NOC (1980–2004), and OAflux (1958–2010)

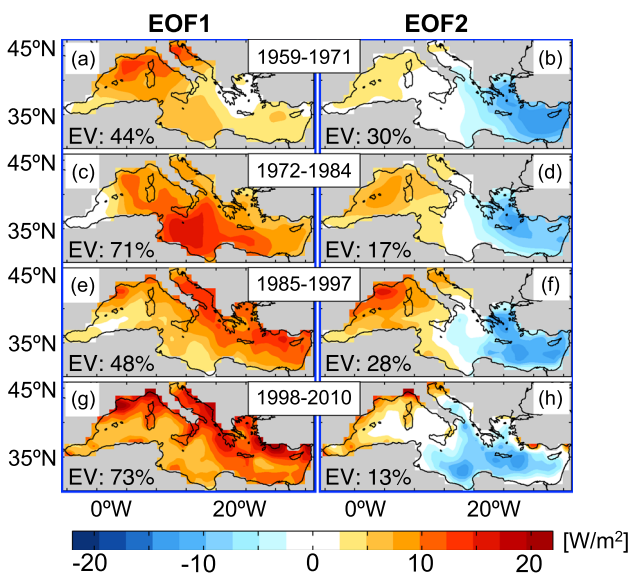

Fig. 11 EOF1 and EOF2 of winter LHFa for OAflux dataset computed over different periods: **a**, **b** 1959–1971; **c**, **d** 1972–1984; **e**, **f** 1985–1997; **g**, **h** 1998–2010. Units are in [W/m^2]

rapid change in the time series may suggest a non-stationary statistic for LHF. As both NOC and the models do not cover this period, we cannot use them to support or contrast this hypothesis. However, we test the stationary time series by splitting the 52-year long OAflux data into 13-year subperiods and re-computing the EOF analysis in each period (Fig. 11). The comparison of the second modes of all of these periods reveals a substantial difference in the EOF2 pattern of the last sub-period (1998–2010), which does no longer shows the characteristic dipole pattern and in which the explained variance drops to 7 %. We also note that by excluding this period from the OAflux EOF decomposition, we find an explained variance for the EOF2 of 26 %, which is close to what is explained by the ENSm-EOF2 (27 %). Far from being conclusive, this observed change in the EOF2 structure during the 1998 to 2010 period may suggest a recent change in the climate controls of this region. The high number of years with anomalies resembling the dipole structure (e.g., spatial correlations as high as 0.80) is an indication that this statistical mode is an expression of a real physical mechanism. In the next section, we explore the forcing dynamics that lead to the DM.

4.2 What mechanism controls the dipole mode?

From the previous analysis, we conclude that the DM is a recurrent physical structure in the Mediterranean Sea and controls an important fraction of the spatial and temporal variability of the LHF anomalies. Josey et al. (2011) used a regression analysis to relate this dipole structure to the EA/WR pattern and hypothesized that "the EA/WR pattern produces a northerly flow of cold dry air over the eastern basin and a southerly flow of relatively warm moist air over the western basin, leading to significant heat flux anomalies that are opposite in sign." Following this hypothesis, we perform a budget analysis to reconstruct the contribution of winds, humidity, and sea surface temperature on the LHF field using a bulk formula. The bulk

formula consists of physical parameterizations that generally relate SST and atmospheric boundary layer variables with air-sea exchange fluxes of heat, momentum, and mass (e.g., Josey et al. 1999; Vickers and Mahrt 2006). In particular, we estimate the LHF field from wind speed ($|\vec{u}|$), 2 m air specific humidity (Qa), and SST. We examine this relationship to quantify the contribution of each to the generation of the DM. We isolate each variable contribution by computing the "partial" composites of LHF anomalies for years (the winter season) when the DM is most active. We obtain these partial composites by calculating the LHF field using the composite for one variable and the climatologies of the other two. With this approach, the reconstructed LHF field will retain the contributions to the DM resulting from a particular variable, allowing its quantification by subtracting the partial LHF composite from the total LHF composite. For the composite, we select years in which the absolute value of the PC2 was above a threshold value set to 1.3, and then we subtract the average field of the positive years from the average field of the negative years. For this analysis, we use the RCMs, the ENSm, and the OAflux observational dataset, which does not provide $|\vec{u}|$; as a result, we obtain this variable from the NCEP dataset (reanalysis).

Before presenting the parameter-specific contributions to the DM, we verify that our bulk formula can effectively reconstruct the LHF field. In Fig. 12, the first column shows the winter LHFa composite while the second column shows the same field but reconstructed using the bulk formula with the composites of $|\vec{u}|$, Qa, and SST. Despite some minor differences, these two columns are similar and therefore, we conclude that the reconstruction is successful. It is worth mentioning that the DM composite pattern of the models can differ. For instance, OURANOS shows a weak dipole while ETZH shows a strong dipole. We present the specific contributions of $|\vec{u}|$ and Qa to the DM mode in the third and in the fourth columns, respectively, of Fig. 12. This figure does not show the SST contribution to the LHFa composite, as this is significantly smaller than $|\vec{u}|$ and Qa contributions. While $|\vec{u}|$ and Qa are the dominant contributors to the east–west anomaly of opposite signs, their contributions differ. In both the observation and the ENSm, the LHF reconstruction composite obtained using Qa anomalies, produces strong negative LHF anomalies in a range of -15 to -20 W/m^2 in the eastern basin and weak positive anomalies in a range of 5 to 10 W/m^2 in the western basin. This spatial pattern closely resembles the corresponding DM presented in the second column of Fig. 12 and the EOF2 patterns of Fig. 7. The LHF reconstruction composite obtained using the $|\vec{u}|$ composite produces negative anomalies in a range of -3 to -7 W/m^2 in the eastern basin and positive anomalies of 5 to 10 W/m^2 in the western basin. This pattern accounts for the amplitude of the positive anomalies in the western basin. This analysis helps us identify specific humidity as an important contributor to the DM. In the next section, we investigate the mechanism controlling the Qa in the OAflux observational dataset.

Fig. 12 LHFa composites. Bulk formula reconstruction of the LHF anomalies using combination of climatological and composite fields of SST, wind speed ($|\vec{u}|$), and 2 m air specific humidity (Qa). For the composite, we selected years where the absolute value of the PC2 were above a threshold value set to 1.3 units. Then we subtracted the average field of the positive years to the average field of the negative years. The first column shows the LHFa composite computed directly from the dataset (no bulk formula is used) while the second column shows the reconstruction using all composite fields. In the third and fourth column, only one composite filed is used for each reconstruction, respectively, ($|\vec{u}|$), and Qa. For the OAflux reconstruction we used ($|\vec{u}|$) from NCEP reanalysis. Units are [W/m^2]

4.2.1 What mechanism controls the Qa?

The LHF reconstruction exercise reveals that both winds and relative humidity play an important role in the formation of the DM. However, the role of winds is likely not limited to direct effects on the LHF. If we examine a composite of wind direction anomalies during DM, we find southerly winds over the western basin and northerly winds over the eastern basin (Fig. 13a). As we have hypothesized, this dipole in the wind direction has an indirect effect on the LHF through the horizontal advection dynamics of the Qa (e.g., transporting dryer northern air over the eastern basin and wetter southern air over the western basin during the positive phase of the DM). The rate of change of Qa associated with changes in horizontal advection is

$$\left.\frac{\partial Q_a}{\partial t}\right|_{ADV} = -\vec{u}_H \cdot \nabla_H Q_a - \frac{Q_a}{\tau} \tag{1}$$

where $\vec{u}_H$ and $\nabla_H Q_a$ denote the horizontal wind vector and the horizontal gradient of Q_a, respectively, and the second term on the right represents the dissipation of the specific humidity with timescale τ. If we split both wind field and specific humidity into both a mean component, or climatological component, and a fluctuation around the mean state, or an anomaly with respect to the climatology, we derive

$$Q_a = Q_a^{clm} + Q_a^{ano} \tag{2a}$$

$$\vec{u}_H = \vec{u}_H^{clm} + \vec{u}_H^{ano} \tag{2b}$$

Combining (1), (2a), and (2b), and neglecting the second-order term, $\vec{u}_H^{ano} \cdot \nabla_H Q_a^{ano}$, we obtain

$$\left.\frac{\partial Q_a^{ano}}{\partial t}\right|_{ADV} = -\vec{u}_H^{clm} \cdot \nabla_H Q_a^{ano} - \vec{u}_H^{ano} \cdot \nabla_H Q_a^{clm} - \frac{Q_a^{ano}}{\tau} \tag{3}$$

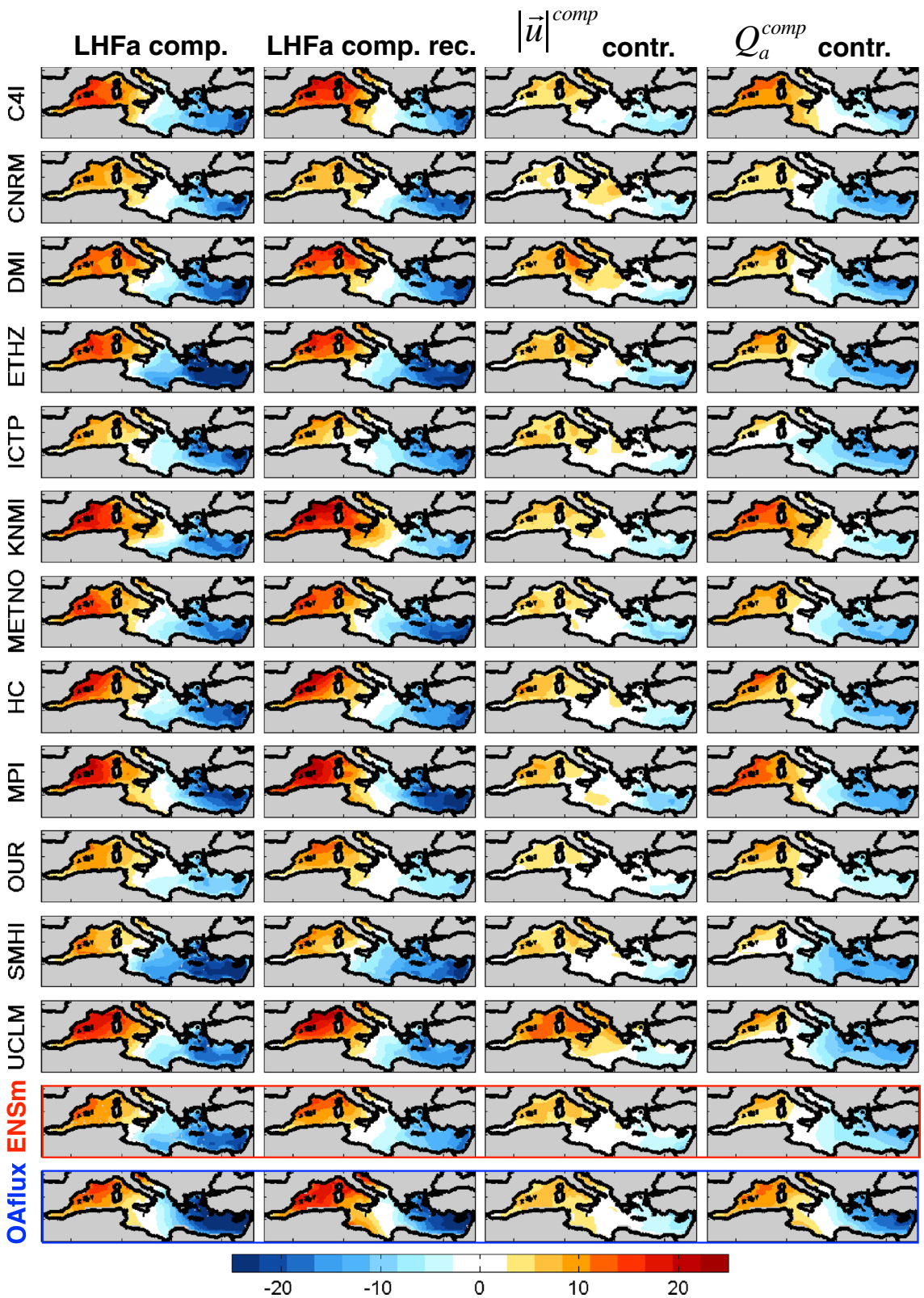
LHFa comp.
LHFa comp. rec.
$|\vec{u}|^{comp}$ contr.
Q_a^{comp} contr.
C4I
CNRM
DMI
ETHZ
ICTP
KNMI
METNO
HC
MPI
OUR
SMHI
UCLM
ENSm
OAflux
-20
-10
0
10
20

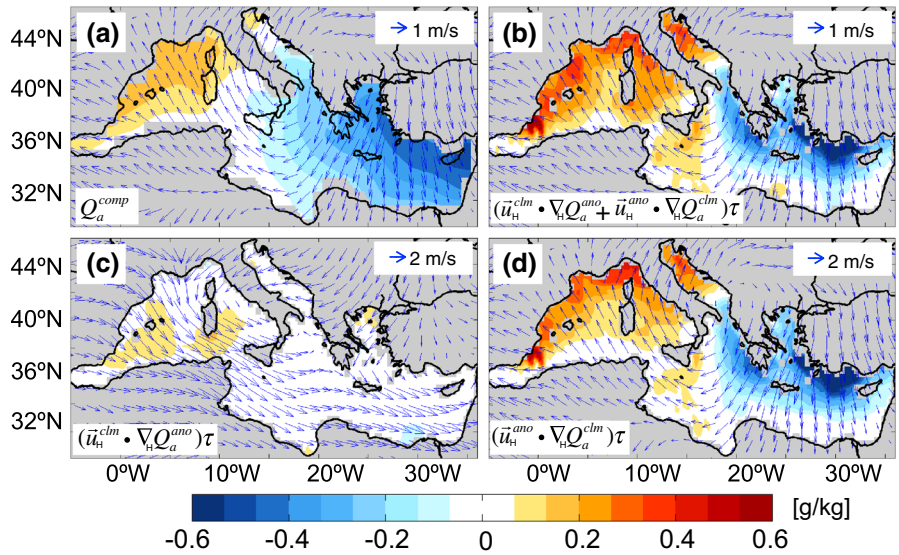

Fig. 13 **a** Specific humidity anomaly composite for years of strong-phase DM. **b** Specific humidity anomaly computed using Eq. 4 with τ = 12 h. **c**, **d** show the two terms of the right hand side of Eq. 4 representing the mean advection of the specific humidity anomaly and of the anomalous advection of the mean specific humidity, respectively. In this analysis, we used 2 m air specific humidity from OAflux, and 10 m wind components from NCEP reanalysis. Units are in [g kg^2]

This equation can be interpreted as follows. The rate of change of the *Qa* anomaly resulting from advection processes is the sum of two contributions: the mean advection of the *Qa* anomaly and an anomalous advection of the mean specific humidity.

Given that $\partial t \ll \tau$, the dominant balance in Eq. 3, obtained by setting the right-hand side to zero, results in an explicit solution for the specific humidity:

$$Q_a^{ano} \approx [-\vec{u}_H^{clm} \cdot \nabla_H Q_a^{ano} - \vec{u}_H^{ano} \cdot \nabla_H Q_a^{clm}] \cdot \tau \qquad (4)$$

To evaluate the contribution of each advective component to the *Qa* tendency associated with the DM, we define the anomalous terms of Eq. 4 using the composites of values during years in which the DM was strong. Furthermore, to optimize the fit of Eq. 4 when reconstructing the DM-driven Q_a^{ano} (Fig. 13a, b), the dissipation timescale is set to $\tau = 0.5$ days, which lies within the range of the dissipation timescales ($\tau_{min} = 6$ h, $\tau_{max} = 3$ days, $\tau_{mean} = 1$ day) estimated from the auto-decorrelation function of six-hourly specific humidity data over the Mediterranean. A comparison of the advection contributions (Fig. 13c, d) reveals that anomalous advection dominates the spatial structure and size of the Q_a^{ano} (Fig. 13a). Large values of the anomalous advection term $\vec{u}_H^{ano} \cdot \nabla_H Q_a^{clm}$ are due to the component of anomalous wind circulation oriented normal to the mean gradient of Q_a^{clm}. This finding is consistent with our initial hypothesis: that changes in winds play an even more important indirect role in the LHF dipole by influencing the advection dynamics of the *Qa*. Although this analysis does not constitute a full budget of the *Qa*, it does suggest that wind-induced anomalous advection is a major contributor to the dipole in *Qa*.

5 Summary and discussion

In this work, we used two observational datasets, OAflux and NOC, and an ensemble of 12 RCMs from the EU-FP6 ENSEMBLES to investigate the dynamics of winter heat flux variability in the Mediterranean Basin from interannual to decadal time scales during 1958 to 2011. We described the first two leading modes as they appear in both observational and model data, and then we studied how they are connected with the most relevant atmospheric modes of variability for the Mediterranean region. The first few EOFs of NHF and LHF were strongly correlated (R = ~0.99) and the LHF dominated NHF spatial and temporal variability (Figs. 1, 2). Thus, our analysis focused on identifying the dynamics controlling the two dominant modes of LHF variability, which explains about ~80 % of the total variance (e.g., Papadopoulos et al. 2012b; Ruiz et al. 2008; Zveryaev and Hannachi 2011) (Figs. 4, 7).

The first mode of LHF has been characterized by a monopole and reflects coherent variations over the entire Mediterranean Basin. Depending on the datasets, this mode explains about 40–60 % of the total variance. Its temporal variability, which tracks the domain average fluctuations of LHF (up to R = 0.99, see Fig. 5), is strongly correlated with the atmospheric variability of the EA (R = 0.5) (Zveryaev and Hannachi 2011). However, we found that the PC1 of LHF exhibited, after 1990, a clear trend not visible in the EA index. The nature of this LHF trend has been attributed to SST-driven changes in the surface humidity gradient linked to global warming (Mariotti 2010; Skliris et al. 2011). Moreover, using six-year low- and high-pass filtered time series on the detrended data, we found (Fig. 6) that the dynamical link between the first mode and the EA

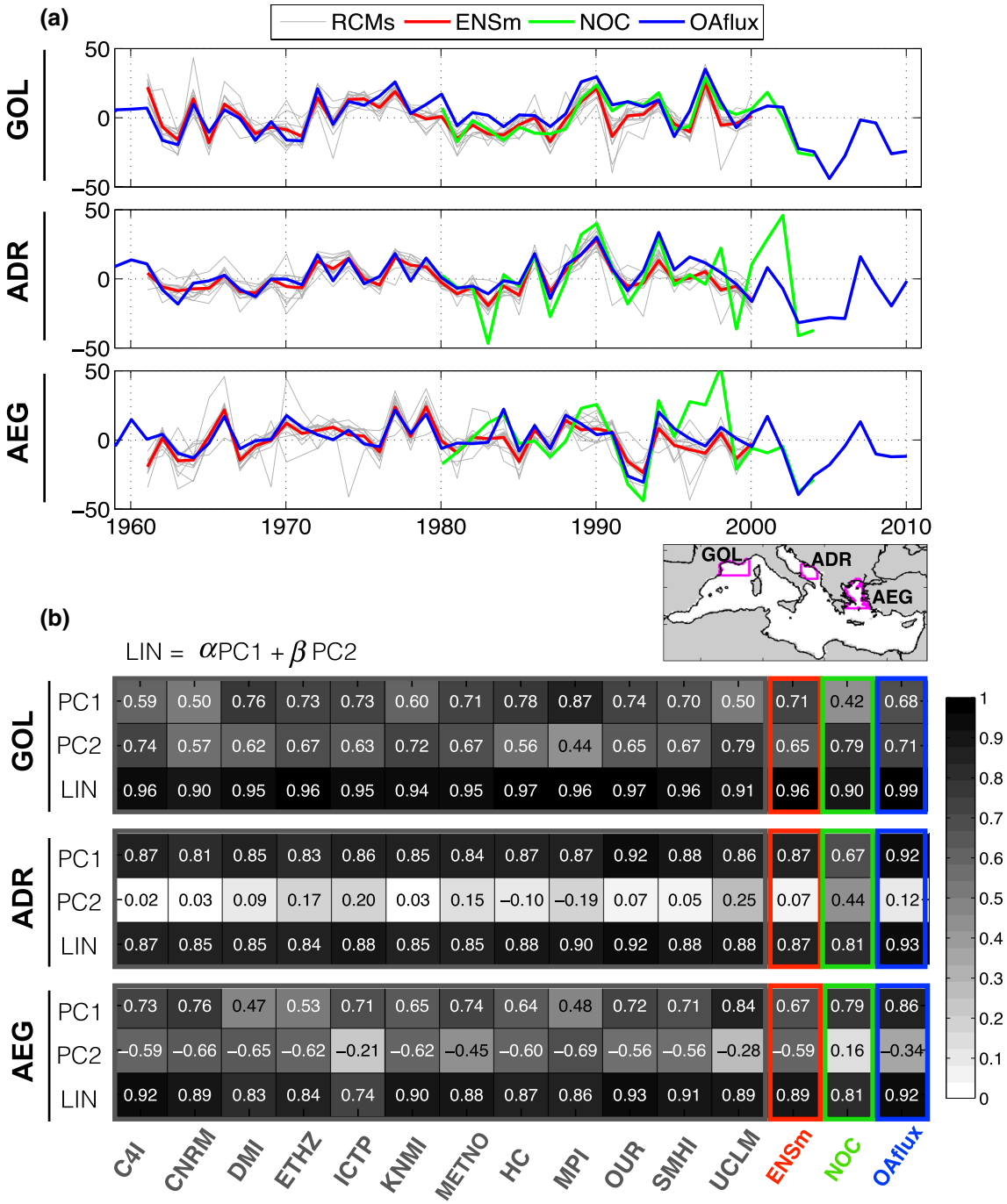

Fig. 14 Variability over the convection regions. **a** Time series of winter LHF anomalies for observations, models, and ENSm, in the three main dense water formation regions: Gulf of Lion (GOL), southern Adriatic Sea (ADR), and Aegean Sea (AEG). **b** Correlation between the first two leading PCs and the time series presented in (**a**). The "LIN" raw shows the correlation between the box-averaged winter LHF anomalies and the best linear model obtained by linearly combining the first two PCs. The magenta outlined regions in the map between Figs. **a** and **b** show the areas chosen for the calculation of the box-averaged time series shown in (**a**). In the subfigure (**a**) units are in [W/m^2]

slightly decreased at high frequencies while it increased at low frequencies.

In contrast to the first mode, the second mode (i.e., DM) of LHF does not show any trend and has been characterized by a well-defined dipole structure, which represents opposite variations of LHF in the eastern and western Mediterranean Sea basins. Depending on the datasets analyzed this mode explains from 16 to 26 % of the total variance. The

analysis of the LHF PC2 revealed a significant correlation with the EA/WR index, which to the best of our knowledge is a new finding. While previous studies have characterized this DM statistically, we explored the spatial relevance and forcing dynamics of the mode. Given that the dipole could emerge statistically as an orthogonal pattern to the first EOF, we assessed the relevance of this mode examining how often the DM explains the spatial structure of the observed interannual anomalies of LHF. Our analysis revealed that despite the DM accounts only for about one-fifth of the total variance, the spatial pattern of LHF winter anomaly is often determined by the phase of the second mode, which recurrently shows spatial correlations with observations above R = 0.80 (Fig. 10).

To understand the mechanism responsible for the generation of the DM, we performed a budget analysis of the LHF winter anomalies using bulk formulas. We found that the main driver of the dipole structure is associated with changes in the regional atmospheric circulation of EA/WR mode. Changes in the winds impact the LHF primarily through the specific humidity and wind speed (Fig. 12). The changes in specific humidity are controlled by the EA/WR wind-induced anomalous advection of cold (dry) air masses from the northeast and warm (moist) air masses from the southwest (Fig. 13). Although this work focuses on statistically derived modes of LHFa, there are direct connections between these modes and fundamental processes, such as the deep water formation in the main convection regions occurring, occurring in the basin. To establish a relationship between the results of our EOF analysis and the deep water formation, we examined the time series of the winter latent heat flux in the convection regions defined as in Josey et al. (2011). There are three specific regions in the Mediterranean Sea where dense water formations occur: the Gulf of Lions (GOL), the Aegean Sea (EAG), and the southern Adriatic Sea (ADR). Figure 14a shows the time series of the box-averaged LHFa for both observations and models. Except for the GOL region, and similar to most of the analyses performed in this work, OAflux and ENSm are highly correlated while NOC shows some major differences. Most of the models (grey curves of Fig. 14a) are close to the ENSm in all the regions analyzed and the inter-model spread is significant only for few models and only during few specific winters. Overall, the simulations are consistent with OAflux observations.

To assess the importance of the first two basin modes of LHFa in the air-sea heat exchange over the convection regions, we computed the correlation between the box-averaged time series and the first two PCs (Fig. 14b). In addition, we estimated the total variance explained by these two modes by computing the correlation between these box-averaged anomalies and the best fitting model obtained by linearly combining the PCs (LIN, LIN = α PC1 + β PC2, where α and β are two fitting parameters determined by solving the least square problem). For both observations and models, the two leading modes show large loading in the GOL region (Figs. 4, 7); therefore, it is not surprising that both PCs, and thus the LIN models, are significantly correlated with the LHFa times series in that region. The correlation for OAflux and ENSm is about 0.70 for both PCs, and it increases to 0.96 for the LIN model of OAflux and 0.99 for that of ENSm. Excluding the NOC dataset, in the Aegean Sea region we found significant correlations for PCs of OAflux, ENSm, and most of the models. However, in this region, the PC1 is more strongly correlated than PC2 (e.g., for OAflux, R = 0.86 for PC1 and R = −0.34 for PC2), which shows negative correlations that are consistent with the dipole nature of the second mode. The situation is different for the ADR region, where, except for the NOC dataset, PC1 shows the highest correlation among the all the convection regions considered, and PC2 is never significantly correlated. The last result is not surprising if one considers that in the ADR region the EOF2 loading is almost null (Fig. 7). In conclusion, the LHFa time series in the convection regions are tightly connected to the first two leading modes of LHFa, which when combined (i.e., LIN model) explain most of the LHF variability in the convection regions.

We note that the DM structure has weakened during the last decades (1996–2010) and its pattern appears less frequently in the LHF anomaly maps (Fig. 10, OAflux). Further analyses using EOFs reveal that the statistics of the DM are no longer stationary after the 1990s, and the DM no longer emerges as the second mode. Given the important role that the DM plays in determining the pattern of LHF anomalies, which in turn is an important factor controlling the deep water formation (e.g., Josey 2003), understanding significance and dynamics of these decadal changes in the DM may enhance our predictability of the Mediterranean climate. Furthermore, previous studies report how this region is one of the climate change hot-spots highlighted by the IPCC simulations (de Sherbinin 2014; Giorgi 2006). Further analyses, for example of MedCORDEX and CMIP5 climate models, are required to explore if these recent decadal changes in the DM are linked to climate change or natural internal variability.

References

Alexander MA, Blade I, Newman M, Lanzante JR, Lau NC, Scott JD (2002) The atmospheric bridge: the influence of ENSO teleconnections on air-sea interaction over the global oceans. J Climate 15:2205–2231. doi:10.1175/1520-0442(2002)015<2205:Tabtio>2.0.Co;2

Andersson A, Bakan S, Fennig K, Grassl H, Klepp C-P, Schulz J (2007) Hamburg ocean atmosphere parameters and fluxes from

satellite data—HOAPS-3—monthly mean. World Data Center Climate. doi:10.1594/WDCC/HOAPS3_MONTHLY

Artale V, Calmanti S, Malanotte-Rizzoli P, Pisacane G, Rupolo V, Tsimplis M (2006) The Atlantic and the Mediterranean Sea as connected systems. Mediterranean climate variability, vol 4. Elsevier, Amsterdam

Bhöm U, Küchen M, Ahrens W, Block A, Hauffe D, Keuler K, Rockel B, Will A (2006) CLM-the climate version of LM: brief description and long-term applications. COSMO Newslett n6

Bignami F, Marullo S, Santoleri R, Schiano ME (1995) Longwave radiation budget in the Mediterranean-Sea. J Geophys Res-Oceans 100:2501–2514. doi:10.1029/94jc02496

Bueh C, Nakamura H (2007) Scandinavian pattern and its climatic impact. Q J Roy Meteor Soc 133:2117–2131. doi:10.1002/Qj.173

Calmanti S, Artale V, Sutera A (2006) North Atlantic MOC variability and the Mediterranean outflow: a box-model study. Tellus A 58:416–423. doi:10.1111/J.1600-0870.2006.00176.X

Christensen JH, Christensen OB, Lopez P, van Meijgaard E, Botzet M (1996) The HIRHAM4 regional atmospheric climate model. Danish Meteorological Institute Scientific Report 96–4, Copenhagen

Collins M, Booth BBB, Harris GR, Murphy JM, Sexton DMH, Webb MJ (2006) Towards quantifying uncertainty in transient climate change. Clim Dyn 27:127–147. doi:10.1007/s00382-006-0121-0

de Sherbinin A (2014) Climate change hotspots mapping: what have we learned? Clim Change 123(1):23–37

Dommenget D, Latif M (2003) Comments on "A cautionary note on the interpretation of EOFs". Reply J Climate 16:1094–1097. doi:10.1175/1520-0442(2003)016<1094:R>2.0.Co;2

Garrett C, Outerbridge R, Thompson K (1993) Interannual variability in Mediterranean heat and buoyancy fluxes. J Climate 6:900–910. doi:10.1175/1520-0442(1993)006<0900:Ivimha>2.0.Co;2

Gilman C, Garrett C (1994) Heat-flux parameterizations for the Mediterranean-Sea—the role of atmospheric aerosols and constraints from the water-budget. J Geophys Res-Oceans 99:5119–5134. doi:10.1029/93jc03069

Giorgi F (2006) Climate change hot-spots. Geophys Res Lett. doi:10.1029/2006gl025734

Giorgi F, Mearns LO (1999) Introduction to special section: regional climate modelling revisited. J Geophys Res (Atmos) 104:6335–6352. doi:10.1029/98JD02072

Haines K, Wu PL (1995) A modelling study of the thermohaline circulation of the Mediterranean Sea: water formation and dispersal. Oceanol Acta 18:401–417

Haugen JE, Haakensatd H (2006) Validation of HIRHAM version 2 with 50 km and 25 km resolution. RegClim General Technical Report, No. 9, pp 159–173

Herrmann MJ, Somot S (2008) Relevance of ERA40 dynamical downscaling for modeling deep convection in the Mediterranean Sea. Geophys Res Lett. doi:10.1029/2007gl032442

Hurrell JW (1995) Decadal trends in the North-Atlantic oscillation—regional temperatures and precipitation. Science 269:676–679. doi:10.1126/science.269.5224.676

Jacob D (2001) A note to the simulation of the annual and interannual variability of the water budget over the Baltic Sea drainage basin. Meteorol Atmos Phys 77:61–73

Josey SA (2003) Changes in the heat and freshwater forcing of the eastern Mediterranean and their influence on deep water formation. J Geophys Res. doi:10.1029/2003jc001778

Josey SA, Kent EC, Taylor PK (1999) New insights into the ocean heat budget closure problem from analysis of the SOC air-sea flux climatology. J Climate 12:2856–2880. doi:10.1175/1520-0442(1999)012<2856:Niitoh>2.0.Co;2

Josey SA, Somot S, Tsimplis M (2011) Impacts of atmospheric modes of variability on Mediterranean Sea surface heat exchange. J Geophys Res. doi:10.1029/2010jc006685

Kalnay E et al (1996) The NCEP/NCAR 40-year reanalysis project. Bull Am Meteorol Soc 77:437–471

Kjellström E, Bärring L, Gollvik S, Hansson U, Jones C, Samuelsson P, Rummukainen M, Ullersig A, Willen U, Wyser K (2005) A 140-year simulation of European climate with the new version of the Rossby Centre regional atmospheric climate model (RCA3). Reports Meteorology and Climatology, vol 108, SMHI, SE-60176 Norrköping, Sweden, 54 pp

Krichak SO, Kishcha P, Alpert P (2002) Decadal trends of main Eurasian oscillations and the Eastern Mediterranean precipitation. Theor Appl Climatol 72:209–220. doi:10.1007/s007040200021

Lascaratos A, Roether W, Nittis K, Klein B (1999) Recent changes in deep water formation and spreading in the eastern Mediterranean Sea: a review. Prog Oceanogr 44:5–36. doi:10.1016/S0079-6611(99)00019-1

Lenderink G, van der Hurk B, van Meijgaard E, van Ulden A, Cujipers H (2003) Simulation of present day climate in RACMO2: first results and model developments. Technical report no 252, KNMI, 24 pp

Madec G, Chartier M, Delecluse P, Crepon M (1991) A 3-dimensional numerical study of deep-water formation in the Northwestern Mediterranean-Sea. J Phys Oceanogr 21:1349–1371

Mariotti A (2010) Recent changes in the Mediterranean water cycle: a pathway toward long-term regional hydroclimatic change? J Climate 23:1513–1525. doi:10.1175/2009jcli3251.1

North GR, Bell TL, Cahalan RF, Moeng FJ (1982) Sampling errors in the estimation of empirical orthogonal functions. Mon Weather Rev 110:699–706. doi:10.1175/1520-0493(1982)110<0699:Seiteo>2.0.Co;2

OrtizBevia MJ, Alvarez-Garcia FJ, de Elvira AR, Liguori G, Carretero JH (2012) The Western Mediterranean summer variability and its feedbacks. Clim Dynam 39:3103–3120. doi:10.1007/s00382-012-1409-x

Papadopoulos VP, Josey SA, Bartzokas A, Somot S, Ruiz S, Drakopoulou P (2012a) Large-scale atmospheric circulation favoring deep- and intermediate-water formation in the Mediterranean Sea. J Climate 25:6079–6091. doi:10.1175/Jcli-D-11-00657.1

Papadopoulos VP, Kontoyiannis H, Ruiz S, Zarokanellos N (2012b) Influence of atmospheric circulation on turbulent air-sea heat fluxes over the Mediterranean Sea during winter. J Geophys Res-Oceans. doi:10.1029/2011jc007455

Plummer D, Caya D, Coté H, Frigon A, Biner S, Giguère M, Paquin D, Harvey R, de Elia R (2006) Climate and climate change over North America as simulated by the Canadian Regional Climate Model. J Clim 19:3112–3132

Rahmstorf S (1996) On the freshwater forcing and transport of the Atlantic thermohaline circulation. Clim Dynam 12:799–811. doi:10.1007/S003820050144

Rahmstorf S (1998) Influence of Mediterranean Outflow on climate Eos. Trans Am Geophys Union 79:281–282. doi:10.1029/98EO00208

Radu R, Déqué M, Somot S (2008) Spectral nudging in a spectral regional climate model. Tellus A 60:898–910

Roether W et al (1996) Recent changes in eastern Mediterranean deep waters. Science 271:333–335

Roether W, Klein B, Manca BB, Theocharis A, Kioroglou S (2007) Transient Eastern Mediterranean deep waters in response to the massive dense-water output of the Aegean Sea in the 1990s. Prog Oceanogr 74:540–571. doi:10.1016/j.pocean.2007.001

Ruiz S, Gomis D, Sotillo MG, Josey SA (2008) Characterization of surface heat fluxes in the Mediterranean Sea from a 44-year high-resolution atmospheric data set. Global Planet Change 63:258–274. doi:10.1016/j.gloplacha.2007.12.002

Sanchez E, Gallardo C, Gaertner MA, Arribas A, Castro M (2004) Future climate extreme events in the Mediterranean simulated

by a regional climate model: a first approach. Glob Plan Chan 44:163–180

Sanchez-Gomez E, Somot S, Josey SA, Dubois C, Elguindi N, Déqué M (2011) Evaluation of Mediterranean Sea water and heat budgets simulated by an ensemble of high resolution regional climate models. Clim Dynam 37:2067–2086. doi:10.1007/s00382-011-1012-6

Schroeder K, Ribotti A, Borghini M, Sorgente R, Perilli A, Gasparini GP (2008) An extensive western Mediterranean deep water renewal between 2004 and 2006. Geophys Res Lett. doi:10.1029/2008gl035146

Simmons AJ, Wallace JM, Branstator GW (1983) Barotropic wave-propagation and instability, and atmospheric teleconnection patterns. J Atmos Sci 40:1363–1392. doi:10.1175/1520-0469(1983)040<1363:Bwpaia>2.0.Co;2

Skliris N, Sofianos S, Gkanasos A, Mantziafou A, Vervatis V, Axaopoulos P, Lascaratos A (2011) Decadal scale variability of sea surface temperature in the Mediterranean Sea in relation to atmospheric variability. Ocean Dyn 62:13–30. doi:10.1007/s10236-011-0493-5

Theocharis A, Nittis K, Kontoyiannis K, Papageorgiou E, Balopoulos E (1999) Climatic changes in the Aegean Sea influence the Eastern Mediterranean thermohaline circulation (1986–1997). Geophys Res Lett 26:1617–1620

Uppala SM et al (2005) The ERA-40 re-analysis. Q J Roy Meteor Soc 131:2961–3012

Vickers D, Mahrt L (2006) Evaluation of the air-sea bulk formula and sea-surface temperature variability from observations. J Geophys Res-Oceans. doi:10.1029/2005jc003323

Wallace JM, Gutzler DS (1981) Teleconnections in the geopotential height field during the Northern Hemisphere winter. Mon Weather Rev 109:784–812. doi:10.1175/1520-0493(1981)109<0784:Titghf>2.0.Co;2

Woodruff SD, Diaz HF, Elms JD, Worley SJ (1998) COADS release 2 and metadata enhancements of marine surface flux fields. Phys Chem Earth 23:517–526

Zhang YC, Rossow WB, Lacis AA, Oinas V, Mishchenko MI (2004) Calculation of radiative fluxes from the surface to top of atmosphere based on ISCCP and other global data sets: refinements of the radiative transfer model and the input data. J Geophys Res-Atmos. doi:10.1029/2003jd004457

Zveryaev II, Hannachi AA (2011) Interannual variability of Mediterranean evaporation and its relation to regional climate. Clim Dynam 38:495–512. doi:10.1007/s00382-011-1218-7